



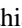



Observation of the quantum shift of a backward rescattering caustic by carrier-envelope phase mapping

Tomoya Mizuno ^{1,*} Nobuhisa Ishii ^{1,†} Teruto Kanai,¹ Philipp Rosenberger ² Dominik Zietlow ²
Matthias F. Kling ^{2,3,‡} Oleg I. Tolstikhin ⁴ Toru Morishita,⁵ and Jiro Itatani¹

¹*The Institute for Solid State Physics, The University of Tokyo, 5-1-5 Kashiwanoha, Kashiwa, Chiba 277-8581, Japan*

²*Physics Department, Ludwig-Maximilians-Universität München, Am Coulombwall 1, D-85748 Garching, Germany*

³*Max Planck Institute of Quantum Optics, Hans-Kopfermann-Str. 1, D-85748 Garching, Germany*

⁴*Moscow Institute of Physics and Technology, Dolgoprudny 141700, Russia*

⁵*Institute for Advanced Science, The University of Electro-communications, 1-5-1 Chofu-ga-oka, Chofu-shi, Tokyo 182-8585, Japan*



(Received 9 March 2021; accepted 15 April 2021; published 29 April 2021)

We study carrier-envelope phase (CEP) -dependent photoelectron momentum distributions (PEMDs) generated by strong-field ionization of Xe atoms with linearly polarized sub-two-cycle near-infrared laser pulses. The PEMDs in the polarization direction end with a cutoff structure whose position and shape are analyzed using the adiabatic theory of rescattering [T. Morishita and O. I. Tolstikhin, *Phys. Rev. A* **96**, 053416 (2017)]. This theory predicts that the cutoff, wherein the PEMD begins to exponentially decay, is located at a quantum caustic that is shifted towards higher energies with respect to the corresponding classical caustic at which long and short backward rescattering trajectories coalesce. The observed position of the cutoff in the PEMDs agrees well with the adiabatic theory, confirming the quantum shift of the caustic. This result paves the way to a more accurate procedure for extracting electron-ion elastic scattering differential cross sections from CEP-dependent cutoffs in strong-field PEMDs.

DOI: [10.1103/PhysRevA.103.043121](https://doi.org/10.1103/PhysRevA.103.043121)

I. INTRODUCTION

According to the three-step model [1,2], an electron released from an atom or molecule by tunneling ionization in a strong laser field is accelerated by the field and then recollides with the parent ion. This recollision may lead to recombination by emitting a high-energy photon, which is the process of high-order harmonic generation (HHG). Or the electron may be elastically or inelastically rescattered and contribute to the photoelectron momentum distribution (PEMD). Each of the processes is crucial in strong-field physics. Thus HHG has become a powerful tool for generating attosecond light pulses [3,4] as well as for probing molecular structure and dynamics [5–9]. Inelastic rescattering allows one to probe the dynamics of molecular dissociation [10–12] and electron correlation in nonsequential double ionization [13–16]. Elastic rescattering imprints valuable information on the electron-ion interaction in the PEMD [17]. Electrons that are rescattered in the forward direction interfere with direct electrons, which have not experienced rescattering. This produces a holographic pattern in the PEMD [18–23] containing the information on the phase of the electron-ion scattering amplitude [22]. The cutoff energy of electrons rescattered in the backward direction provides the information on the carrier-envelope phase (CEP) of the ionizing laser pulse [24–30]. Furthermore, in the vicinity of a backward rescattering cutoff, the PEMD factorizes into

the differential cross section (DCS) for elastic electron-ion scattering and a returning photoelectron wave packet (RWP) [31–36], which allows one to extract the DCS from the PEMD [37–49]. The extraction procedure requires knowing how the position of the cutoff depends on the pulse parameters and the target system. In this paper, we address this issue by experimentally and theoretically investigating backward rescattering cutoff structures in the PEMDs generated by the ionization of Xe atoms with linearly polarized few-cycle infrared pulses.

From an experimental viewpoint, there are two primary factors that introduce uncertainty in the position of the cutoff. First, each half cycle of a laser pulse produces one backward rescattering half cycle cutoff (HCO) in the PEMD with the photoelectron momenta directed opposite to the field. Typical few-cycle pulses contain several half cycles with the same field direction and close field strengths producing overlapping HCO structures in the PEMD. If the different structures are not resolved, the strength of the ionizing field cannot be accurately determined, and hence the DCS cannot be reliably extracted. To overcome this difficulty, we use an optical parametric chirped pulse amplifier that produces sub-two-cycle CEP-stable pulses at 1600 nm [50]. In our preceding work, we have demonstrated that one could experimentally resolve the outermost HCO in PEMDs generated by CEP-stable sub-two-cycle pulses and control its position by varying the CEP [44]. In the present paper, we additionally resolve the adjacent inner HCO in certain intervals of the CEP. Second, the experimental PEMD accumulates photoelectrons that originate from the different parts of the focal volume. The laser intensity is nonuniformly distributed over the volume; therefore, the PEMD collects atomic responses at different intensities, which affects the apparent position of HCOs. However, the

*mizuno.tomoya@issp.u-tokyo.ac.jp

†Present address: Kansai Photon Science Institute, National Institutes for Quantum and Radiological Science and Technology (QST), 8-1-7 Umemidai Kizugawa, Kyoto 619-0215, Japan.

‡matthias.kling@lmu.de and matthias.kling@mpq.mpg.de

outermost HCO is produced by electrons that originate from the region with maximum intensity, ensuring that the PEMD in its vicinity represents almost a single-intensity response. Thus the use of CEP-stable sub-two-cycle pulses and focusing on the outermost HCO enables us to minimize the uncertainty in its position.

From a theoretical viewpoint, extracting a DCS from an experimental PEMD requires knowing not only the position of the HCO, but also an explicit form of the RWP. In other words, one needs an analytical theory that describes the structure of the PEMD near an HCO. Such a theory has been developed [36] on the basis of the adiabatic theory [51]. In the present analysis, we use the factorization formula derived in Ref. [36]. The key object in this theory is a *classical* caustic associated with a given HCO at which long and short backward rescattering trajectories coalesce [24]. The position of this caustic in the photoelectron momentum space is completely determined by the laser field and is independent of the target system. Furthermore, the theory introduces the corresponding *quantum* caustic. It is shifted towards higher energies with respect to the classical caustic, and the value of this quantum shift depends on the target. The factorization formula holds in a region including both caustics. The dependence of the PEMD on the component of the photoelectron momentum that is normal to the caustics exhibits a characteristic shape described by the Airy function. The argument of this function turns to zero at the quantum caustic, resulting in the exponential decay beyond this caustic in PEMDs. Therefore, it is the quantum caustic which specifies the meaning and defines the exact position of the HCO. The factorization formula, including the quantum shift of the caustic, was validated quantitatively by comparison with PEMDs obtained by solving the time-dependent Schrödinger equation [36]. A preliminary version of this formula presented in Ref. [44] did not account for the shift; thus it was not included in the analysis of experimental results therein. A more thorough derivation documented in Ref. [36] revealed the shift. The resulting formula was used in the analysis of experimental PEMDs [47,49]. However, because of the uncertainties mentioned above, the shift could not be unambiguously detected. In this paper, we use the advantages of our light source to experimentally verify the quantum shift of the caustic predicted in Ref. [36].

It is worthwhile to mention that a similar quantum shift of the cutoff energy of HHG with respect to that resulting from classical mechanics [1] was predicted theoretically [52–55]. However, in the case of HHG, in addition to the difficulties in resolving a single-intensity cutoff, there exist macroscopic effects, such as phase matching and nonlinear propagation, which significantly affect observable spectra and hinder the extraction of a single-atom response. This makes the experimental verification of the quantum shift of the cutoff in HHG hardly possible, which emphasizes the exclusiveness of obtaining the shift from PEMDs.

The paper is organized as follows. In Sec. II, we present the factorization formula describing the PEMD near a backward rescattering caustic within the adiabatic theory [36]. In Sec. III, we outline the experimental setup and procedure. In Sec. IV, we discuss our experimental and theoretical results. Section V concludes the paper.

II. ADIABATIC THEORY

The structure of strong-field PEMDs near a backward rescattering caustic is analyzed within the adiabatic theory [51] in Ref. [36]. In this section, we briefly introduce basic objects of the theory and then present the factorization formula describing the PEMD.

We assume that the ionizing laser field is linearly polarized along the laboratory z axis, i.e., $\mathbf{F}(t) = F(t)\mathbf{e}_z$. To model the experimental results, we set

$$F(t) = F_0 \exp[-(\sqrt{2 \ln 2} t/T)^2] \cos(\omega t - \phi). \quad (1)$$

Here, we assume a Gaussian envelope, where the laser field is characterized by its amplitude F_0 , duration (full width at half maximum of intensity) T , carrier frequency ω , and CEP ϕ . In the present experiment we use 1600-nm pulses with typical amplitude $F_0 \sim 0.03$ a.u. (intensity $I = cF_0^2/8\pi \sim 3.2 \times 10^{13}$ W/cm², where c is the speed of light), duration $T \sim 13.5$ fs, and CEP ϕ varied continuously. The PEMD generated in the ionization of an atom by such a pulse as a function of the photoelectron momentum \mathbf{k} is axially symmetric about the k_z axis. In the experiment, only a one-dimensional cut of the PEMD along the k_z axis to be denoted by $P(k_z)$ is measured. In the vicinity of a caustic, the function $P(k_z)$ is determined by photoelectrons rescattered exactly in the backward direction. Therefore, we present the factorization formula only for this particular case; the general case of rescattering at an arbitrary angle is treated in Ref. [36].

In the adiabatic regime, strong-field ionization proceeds as if the ionizing field were static and equal to the instantaneous laser field [51]. The unperturbed initial state of a target atom in the presence of a static electric field $\mathbf{F} = F\mathbf{e}_z$ turns into the corresponding Siegert state [56]. All the ionization observables can be described in terms of properties of this state. We need the complex Siegert eigenvalue $E(F) = \mathcal{E}(F) - \frac{i}{2}\Gamma(F)$ defining the Stark-shifted energy $\mathcal{E}(F)$ and ionization rate $\Gamma(F)$ of the state and the amplitude $A(k_\perp; F)$ of the transverse momentum distribution of outgoing electrons in the asymptotic part of the Siegert eigenfunction. The field-free energy of the initial state is $E_0 = E(0)$. Only electrons that tunnel with zero transverse momentum return for rescattering, so we set $k_\perp = 0$. By substituting $F \rightarrow F(t)$, we obtain instantaneous properties of the Siegert state characterizing the target. The present target atom Xe is described in the single-active-electron approximation by the potential defined in Ref. [57]. The energy of the unperturbed $5p$ state of Xe is $E_0 \approx -0.446$ a.u. We calculate the corresponding Siegert state using the method developed in Ref. [56], in the same way as in Ref. [36].

An electron released from a target atom by tunneling may return within one optical cycle to the parent ion and undergo elastic rescattering. The rescattering event is described by the scattering amplitude $f(k, \theta)$ defining the DCS $d\sigma/d\Omega = |f(k, \theta)|^2$, where $k > 0$ is the incident momentum and θ is the scattering angle [58]. Backward rescattering corresponds to $\theta = \pi$; therefore, $f(k, \pi)$ is another property of the target involved in the theory. We calculate it using the same potential as in the calculation of the Siegert state.

After rescattering, the electron flies away with asymptotic momentum \mathbf{k} . In the general case, each half cycle of the

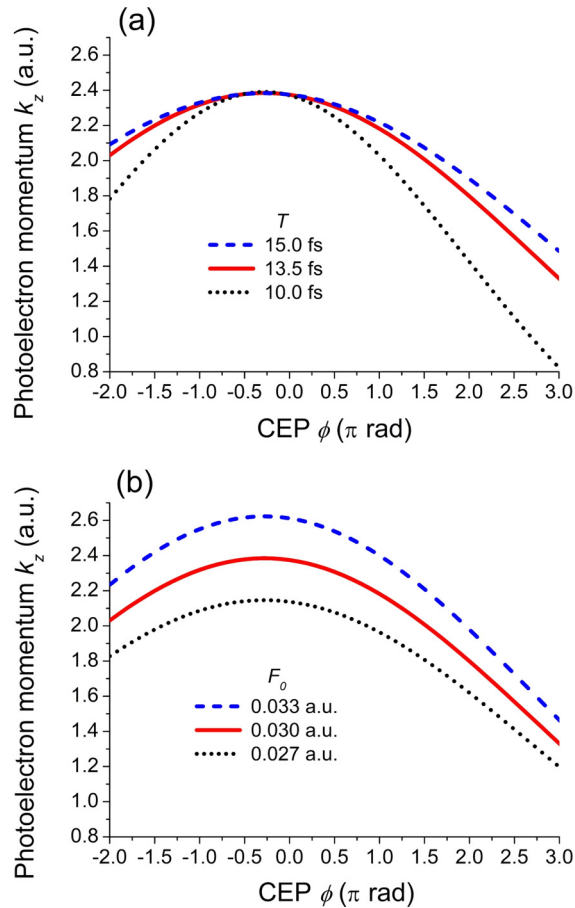


FIG. 1. Classical caustic k_c for pulses defined by Eq. (1) with wavelength of 1600 nm as a function of the CEP ϕ calculated (a) for three pulse durations $T = 10, 13.5,$ and 15 fs at $F_0 = 0.03$ a.u. and (b) for three pulse amplitudes $F_0 = 0.027, 0.03,$ and 0.033 a.u. at $T = 13.5$ fs. This is the outermost caustic in the region $k_z > 0$ at $\phi = 0$.

laser field $F(t)$ produces two different long and short classical rescattering trajectories contributing to the PEMD at the same final \mathbf{k} in a certain region of the photoelectron momentum space. The two trajectories coalesce at the high-energy boundary of the region. Therefore, the boundary is called the classical caustic generated by the given half cycle. There are two classical trajectories contributing to the PEMD on the lower-energy side of the caustic and none on its higher-energy side. The caustic is a surface of revolution about the k_z axis. Let k_c denote the point where it crosses the k_z axis. Let t_i and t_r be the moments of ionization and rescattering and $\mathbf{u}_f = u_f \mathbf{e}_z$ be the incident momentum of rescattering for the coalesced trajectories contributing to the PEMD $P(k_z)$ at $k_z = k_c$. The values of $k_c, t_i, t_r,$ and u_f are completely determined by classical mechanics and the laser field $F(t)$, and hence all are real; explicit equations defining these kinematic characteristics of rescattering are given in Ref. [36].

In the present experiment, we measure the PEMD $P(k_z)$ only at $k_z > 0$. So, we are interested only in positive caustics, $k_c > 0$, with negative momentum of rescattering, $u_f < 0$, generated by negative half cycles of the pulse, $F(t) < 0$. Figure 1 shows the behavior of such a caustic as a function

of the CEP ϕ for laser fields $F(t)$ at 1600 nm with several durations T and amplitudes F_0 defined by Eq. (1). For all the pulses considered, the caustic chosen for the illustration is the outermost caustic in the region $k_z > 0$ at $\phi = 0$. It is generated by the half cycle of $F(t)$ which at $\phi = 0$ occupies the time interval $-3\pi/2 < \omega t < -\pi/2$. As ϕ varies, this half cycle shifts to the left ($\phi < 0$) or right ($\phi > 0$) along the time axis, and the value of k_c changes continuously—this continuous variation is shown in Fig. 1. In addition to the outermost caustic, there are inner caustics generated by half cycles with different amplitude. Note that the set of *all* caustics generated by a pulse defined by Eq. (1) is transformed into itself as ϕ varies by 2π while the other pulse parameters are kept fixed, but each individual caustic generally is not a periodic function of ϕ . Figure 1(a) shows that, except for a small interval near $\phi = 0$, the position of the caustic is rather sensitive to the pulse duration T . Figure 1(b) illustrates similar sensitivity to the pulse amplitude F_0 .

Having introduced and illustrated the classical caustic, we next discuss the corresponding quantum caustic. Within the adiabatic theory, the time integral defining the PEMD in the vicinity of a given classical caustic has two saddle points associated with the long and short rescattering trajectories [36]. However, in addition to the classical term describing propagation along the trajectories, the action in the integrand contains a quantum term $-\int^t E(F(t'))dt'$ that accounts for the evolution of the ionizing Siegert state [51]. The surface in the photoelectron momentum space where the two saddle points of the action including this term coalesce is called the *quantum* caustic. This caustic is shifted with respect to the classical caustic towards higher energies; its position for an arbitrary scattering angle θ is defined in Ref. [36]. The quantum caustic is also a surface of revolution about the k_z axis. Let k_q denote the point where it crosses the k_z axis, which corresponds to $\theta = \pi$. The value of k_q is related to k_c by

$$k_q = k_c + q, \quad (2)$$

where the quantum shift q is given by

$$q = \frac{-E(F(t_i))}{(t_r - t_i)|F(t_i)|}. \quad (3)$$

Note that the shift depends not only on the pulse (defining t_i and t_r), but also on the target. Furthermore, the shift is generally complex because the Siegert eigenvalue $E(F)$ is complex; therefore, the image of the quantum caustic on the real k_z axis is given by the real part of k_q . However, for the present target and pulses the imaginary part of k_q is small and, for simplicity, we disregard it in the discussion. Then the shift is defined by the instantaneous value of the Stark-shifted energy $\mathcal{E}(F(t_i))$ of the initial state at the moment of ionization. The derivation of Eq. (3) assumes that k_c is close to k_q . Indeed, in the adiabatic regime ($\epsilon \ll 1$) the shift q is $O(\epsilon)$, where ϵ is the adiabatic parameter giving the ratio of the target and laser field time scales [36]. In Fig. 2, we illustrate the relative position and behavior of a pair of classical and quantum caustics as functions of the CEP ϕ . We consider the same caustic as in Fig. 1 generated by a pulse with the same parameters as for the middle (red) lines in Fig. 1. The quantum shift between the caustics is clearly seen in the figure.

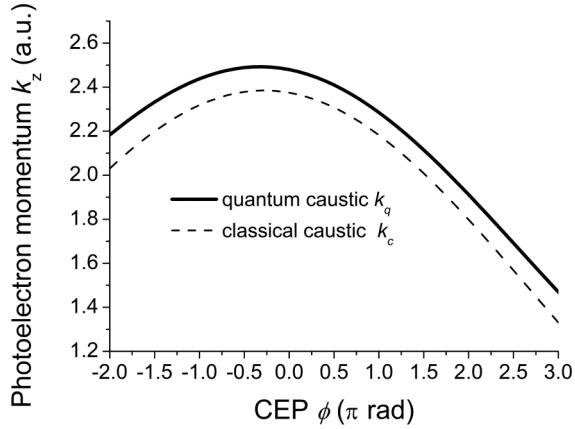


FIG. 2. Classical k_c and quantum k_q caustics for pulses defined by Eq. (1) with wavelength of 1600 nm, amplitude $F_0 = 0.03$ a.u., and duration $T = 13.5$ fs as functions of the CEP ϕ . The classical caustic coincides with the one shown by the middle (red) lines in Fig. 1.

Let us emphasize that the quantum shift given in Ref. [36] can be applied to any amplitude and shape of a laser pulse and scattering angle of a photoelectron. A shift at the scattering angle $\theta = \pi$ obtained from the quantum orbit theory [59,60] is given in the energy domain in Ref. [61]. It agrees with Eq. (3) in the case of a weak monochromatic field. This result of Ref. [61] has been confirmed by the analysis of a zero-range-potential model within the effective range theory [32]. The quantum orbit theory was also applied to the numerical study of CEP-dependent cutoffs for few-cycle pulses [25], but no analytical formula for the shift in this case was given. In Ref. [40], it was suggested on physical grounds to replace the field-free ionization potential in the expression for the shift [61] by the binding energy of a dressed state in a monochromatic laser field, although the replacement was not justified analytically. With such an amendment, the shift from Ref. [61] becomes closer to that in Eq. (3) defined by the Siegert eigenvalue. This approximation holds only for monochromatic fields, as confirmed by the comparison with experimental data [40]. However, the dressed state does not reproduce subcycle dynamics, which is essential for treating the present sub-two-cycle pulses. More details on the treatment of the quantum shift within the quantum orbit theory can be found in Ref. [27].

We can now present the factorization formula. The contribution to the PEMD from a given half cycle in the vicinity of the corresponding classical and quantum caustics is given by [36]

$$P_c(k_z) = |f(|u_f|, \pi)|^2 W(k_z), \quad (4)$$

where the first factor is the DCS for electron-ion elastic scattering with incident momentum $|u_f|$ in the backward direction and the second factor is the RWP,

$$W(k_z) = |\text{Ai}[\alpha(k_z - k_q)]|^2 \left| \frac{2}{S_r'''} \right|^{2/3} \frac{4\pi^2 |A(0; F(t_i))|^2}{(t_r - t_i)^3 |F(t_i)|} \times \exp \left[- \int_{-\infty}^{t_i} \Gamma(F(t)) dt \right]. \quad (5)$$

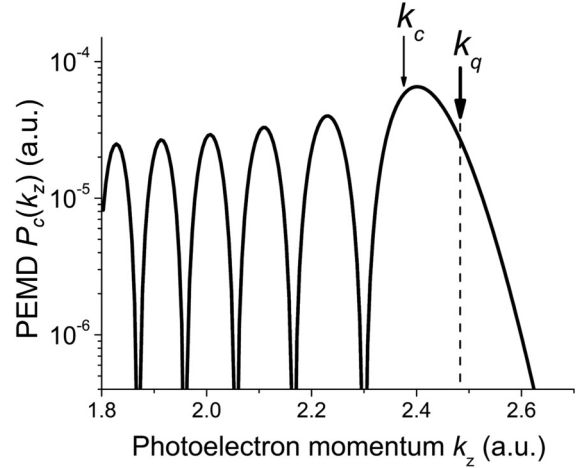


FIG. 3. Contribution to the PEMD defined by Eq. (4) for the Xe atom generated by the same pulse and corresponding to the same caustic as in Fig. 2 at $\phi = 0$. The classical and quantum caustics are indicated by the arrows.

Here $\text{Ai}(z)$ is the Airy function, the coefficient in its argument is given by

$$\alpha = \left| \frac{2}{S_r'''} \right|^{1/3} |u_f|, \quad (6)$$

and S_r''' is the third derivative of the classical action at the moment of rescattering t_r at the caustic defined in Ref. [36]. The conditions of applicability of the factorization formula (4) as well as the numerical results demonstrating its good quantitative performance for a number of targets and pulses can be found in Ref. [36]. The behavior of $P_c(k_z)$ is illustrated in Fig. 3. We show the distribution generated by the same pulse and corresponding to the same caustic as in Fig. 2 at $\phi = 0$. The dependence of $P_c(k_z)$ on k_z is described by the Airy function in Eq. (5); all the other factors in Eqs. (4) and (5) do not depend on k_z . The argument of the Airy function turns to zero at the quantum caustic $k_z = k_q$; hence $P_c(k_z)$ rapidly decays beyond this point. Thus the quantum caustic quantitatively specifies the meaning of a more vague experimental concept of HCO. On the lower-energy side of the caustic, the distribution $P_c(k_z)$ exhibits an oscillatory behavior, which is caused by the interference of individual contributions from two saddle points associated with long and short rescattering trajectories. The shift between the classical and quantum caustics for the pulses shown in Fig. 3 is comparable to the width of the main maximum of the distribution; therefore, neglecting the shift would significantly modify the PEMD. The shift is confirmed by the calculations in Ref. [36].

In the vicinity of the outermost caustic, there are no other contributions to the PEMD except that from the coalescing trajectories described by Eq. (4). Thus the total PEMD $P(k_z)$ coincides with $P_c(k_z)$ in this region. In the vicinity of an inner caustic, there exist additional contributions from other pairs of trajectories that coalesce at the outer caustics. Because the different contributions should be summed up coherently, the structure of $P(k_z)$ in this region may be rather complex. However, if the caustic contribution dominates, the main maximum of the Airy function in Eq. (4) can be resolved in the experiment, and this is what we call the HCO structure.

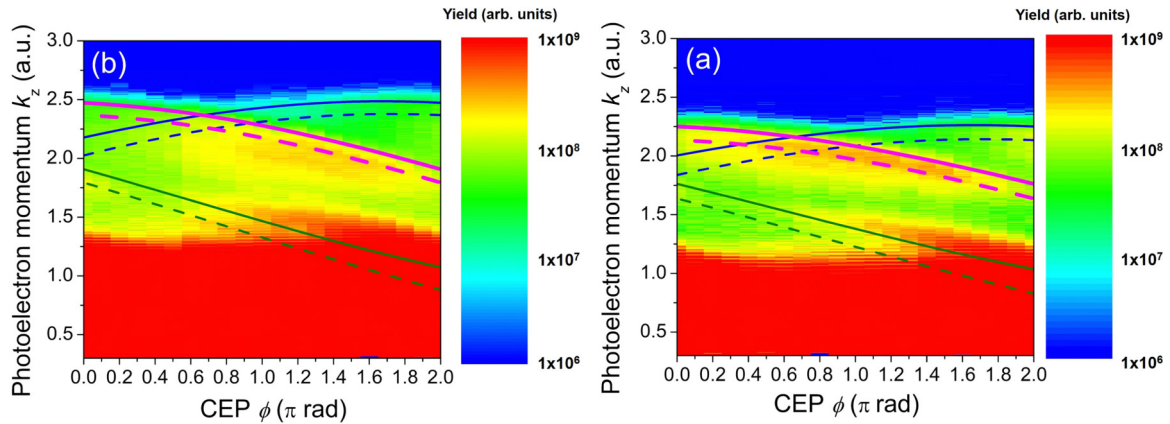


FIG. 4. Measured PEMDs $P(k_z)$ as a function of CEP ϕ at pulse energies of (a) 190 μJ and (b) 210 μJ . Dashed and solid curves represent classical k_c and quantum k_q caustics at the intensities of (a) $2.6 \times 10^{13} \text{ W/cm}^2$ ($F_0 = 0.02722$ a.u.) and (b) $3.2 \times 10^{13} \text{ W/cm}^2$ ($F_0 = 0.03028$ a.u.), and pulse durations of 13.8 fs and 13.5 fs, respectively. The three caustic curves [thin blue (dark gray), thick red, and thin green (light gray)] correspond to three different HCOs that are defined as HCO(-1), HCO(0), and HCO(1), respectively.

III. EXPERIMENT

In our experiment, we measured photoelectron momenta by means of a 760-mm-long time-of-flight (TOF) spectrometer. The polarization direction of the ionizing pulses, which is set to the z axis, is parallel to the TOF axis. Thus the emission angle Θ between the polarization direction and the photoelectron momentum is zero. The detection angle with respect to the TOF axis (the z axis) is limited to approximately 1.5° , corresponding to 2×10^{-3} sr. The linearly polarized few-cycle infrared pulses at the center wavelength of 1600 nm are provided by an optical parametric chirped-pulse amplification system described in [50], which are focused into a target gas using a concave mirror with a focal length of 375 mm (F no. ~ 75). The pulse is compressed to durations around 13.5 fs in the present experiment. The target Xe gas is introduced into the TOF chamber with an effusive source. To avoid the change of the CEP due to the Gouy phase effect, which would otherwise obfuscate the CEP sensitivity, the target position is offset from the focal point with a loose focusing geometry. The CEP is controlled with an acousto-optic programmable dispersive filter (Fastlite, Dazzler HR45-1100-2200 T1). This method of CEP control ensures changing the CEP without affecting the focusing condition and the field envelope. The CEP is scanned in steps of 0.1π rad every 300 s from 0 to 2π rad. In this work, we obtain a PEMD $P(k_z)$ generated in ionization of Xe atoms, which is given in only one dimension along the k_z axis, and only at $k_z > 0$.

Figures 4(a) and 4(b) show obtained CEP-dependent PEMDs $P(k_z)$ from $\phi = 0$ to 2π , at the pulse energies of 190 and 210 μJ , respectively. The total PEMD $P(k_z)$ is a 2π periodic function of the CEP [26,28,44]. This is because the electric field defined by Eq. (1) also has 2π periodicity with respect to the CEP. Therefore, the CEP range of 0 to 2π covers one period of $P(k_z)$.

To determine the peak intensity, the pulse duration, and the absolute CEP, we compare the measured total PEMDs $P(k_z)$ with calculated PEMDs $P_c(k_z)$ from a given half cycle in Sec. IV. Integration of measured $P(k_z)$ in the entire momentum space is just total electron count, which corresponds to

relative probability. This means that the normalization factor of measured $P(k_z)$ to absolute ionization probability is also an unknown parameter.

IV. RESULTS AND DISCUSSIONS

We determine the laser parameters and the normalization factor by comparing the measured PEMDs $P(k_z)$ with the calculated PEMDs $P_c(k_z)$ from a given half cycle using Eq. (4). We assign each individual HCO to the quantum caustic k_q , and discuss the quantum shift of the caustic, which is imprinted on the 2π periodicity of $P(k_z)$.

A. Determination of the laser parameters and normalization factor

As illustrated in Sec. II, the caustic of the highest momentum is approximately generated at $\phi = -0.2\pi$. This is mostly independent of the pulse duration (see Fig. 1). Therefore, the measured HCO of the highest momentum can be assigned to $\phi = -0.2\pi$. Furthermore, except for a small range around $\phi = 0$, the position of the caustic is sensitive to the pulse duration T , the pulse amplitude F_0 (corresponding intensity I), and the CEP ϕ (see Fig. 1). Based on these behaviors, the laser parameters can be determined from the CEP dependence of the caustic position. We fit $P(k_z)$ to $P_c(k_z)$ in the vicinity of the outermost caustic using the limited CEP range of $-0.3\pi \leq \phi \leq 0.7\pi$ to determine the laser parameters and the normalization factor N of $P(k_z)$ to $P_c(k_z)$. The limited CEP range corresponds to the CEP range of $0 \leq \phi \leq 0.7\pi$ and $1.7\pi \leq \phi \leq 2.0\pi$ due to the 2π periodicity of $P(k_z)$. The details of the fitting procedure are described in the Appendix. Here, we briefly provide the fitting result for two experiment sets of pulse energies of 190 and 210 μJ , as shown in Figs. 4(a) and 4(b). The estimated I and T for pulse energies of 190 and 210 μJ are $I = 2.6 \times 10^{13} \text{ W/cm}^2$ ($F_0 = 0.02722$ a.u.) with $T = 13.8$ fs and $I = 3.2 \times 10^{13} \text{ W/cm}^2$ ($F_0 = 0.03028$ a.u.) with $T = 13.5$ fs, respectively.

In Figs. 4(a) and 4(b), we show three classical k_c and quantum k_q caustic curves for different HCOs using the estimated

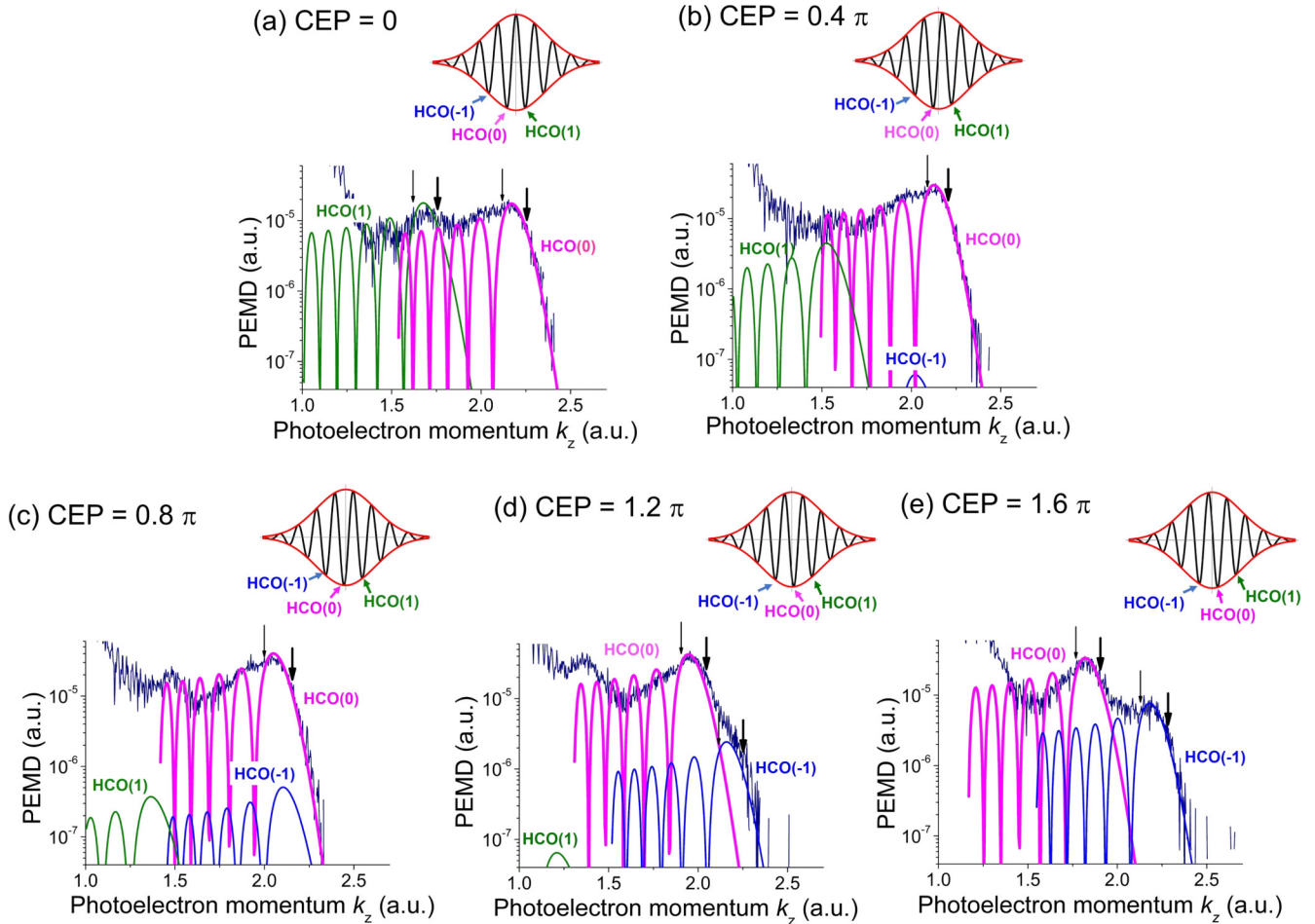


FIG. 5. Measured PEMDs $P(k_z)$ (thin black curves) at selected CEPs ϕ of (a) 0, (b) 0.4 , (c) 0.8 , (d) 1.2 , and (e) $1.6 \times \pi$ at an estimated effective intensity of 2.6×10^{13} W/cm², and a pulse duration of 13.8 fs. The thick red, thin blue (dark gray), and thin green (light gray) curves show calculated PEMDs $P_c(k_z)$ corresponding to a half cycle of the electric field, as depicted in the top figures. Thin and thick arrows indicate the classical k_c and quantum k_q caustics, respectively. The measured PEMDs $P(k_z)$ are normalized by an estimated normalization factor N to match the calculated PEMDs $P_c(k_z)$. Note that we set a common range in the vertical axis for better comparison, which makes blue (dark gray) and green (light gray) curves out of range in some cases.

pulse parameters. Here, we define HCO(n) as the HCO that is generated by the half cycle of $F(t)$ which at $\phi = 0$ occupies the time interval $-3\pi/2 + 2n\pi < \omega t < -\pi/2 + 2n\pi$ (n is an integer number). The red k_c and k_q curves show the caustics for HCO(0), and those depicted in Fig. 4(b) are identical with the caustic curves that are shown in Fig. 2. Moreover, the blue and green caustic curves exhibit those for HCO(-1) and HCO(1), respectively. The specific caustic curves for HCO(0) coincide with those for HCO(n) shifted by $2\pi \times n$. Hence the CEP dependence of HCO(0), as shown in Figs. 1 and 2, has complete information regarding all the caustics generated by the same pulse. The individual caustic HCO(n) shows no 2π periodicity but is encoded in $P(k_z)$ that has 2π periodicity as shown in Figs. 4(a) and 4(b). We observed the HCO(0) in the full CEP range of $\phi = 0$ to 2π , and also observed HCO(-1) in the limited CEP range of $\phi = \pi$ to 2π and HCO(1) at only the CEP of zero. Observed HCOs coincide with HCO(0) in the CEP range of $\phi = -\pi$ to 2π . Thus we obtained the CEP-dependent HCO in the CEP range of $\phi = -\pi$ to 2π , although we measured $P(k_z)$ in the CEP range of $\phi = 0$ to 2π .

The quantum shift is not negligible in the case of the present laser parameters (see Figs. 2–4). If the quantum shift is not considered, the boundary of $P(k_z)$ is regarded as the classical caustic k_c . Actually, in a previous study [44], we fitted the boundary to k_c to extract the laser parameters from the obtained $P(k_z)$. The previous procedure causes significant overestimation of the intensity. For example, if we fit the boundary of $P(k_z)$ for a pulse energy of 190 μ J in Fig. 4(a) to k_c , the intensity I is approximately estimated to be 2.9×10^{13} W/cm² ($F_0 = 0.0285$ a.u.). The error of the estimation is approximately 12% for I . This overestimation of intensity significantly influences the accuracy of the returning wave packet $W(k_z)$ and the rescattering momentum u_f , resulting in uncertainty in the extracted DCS. Therefore, quantum shift is important in the case of the present laser parameters.

B. Comparison between the measured total PEMDs $P(k_z)$ and calculated PEMDs $P_c(k_z)$ from a given half cycle

Figures 5 and 6 show the measured PEMDs $P(k_z)$ and calculated PEMDs $P_c(k_z)$ using Eq. (4) at selected CEPs ϕ

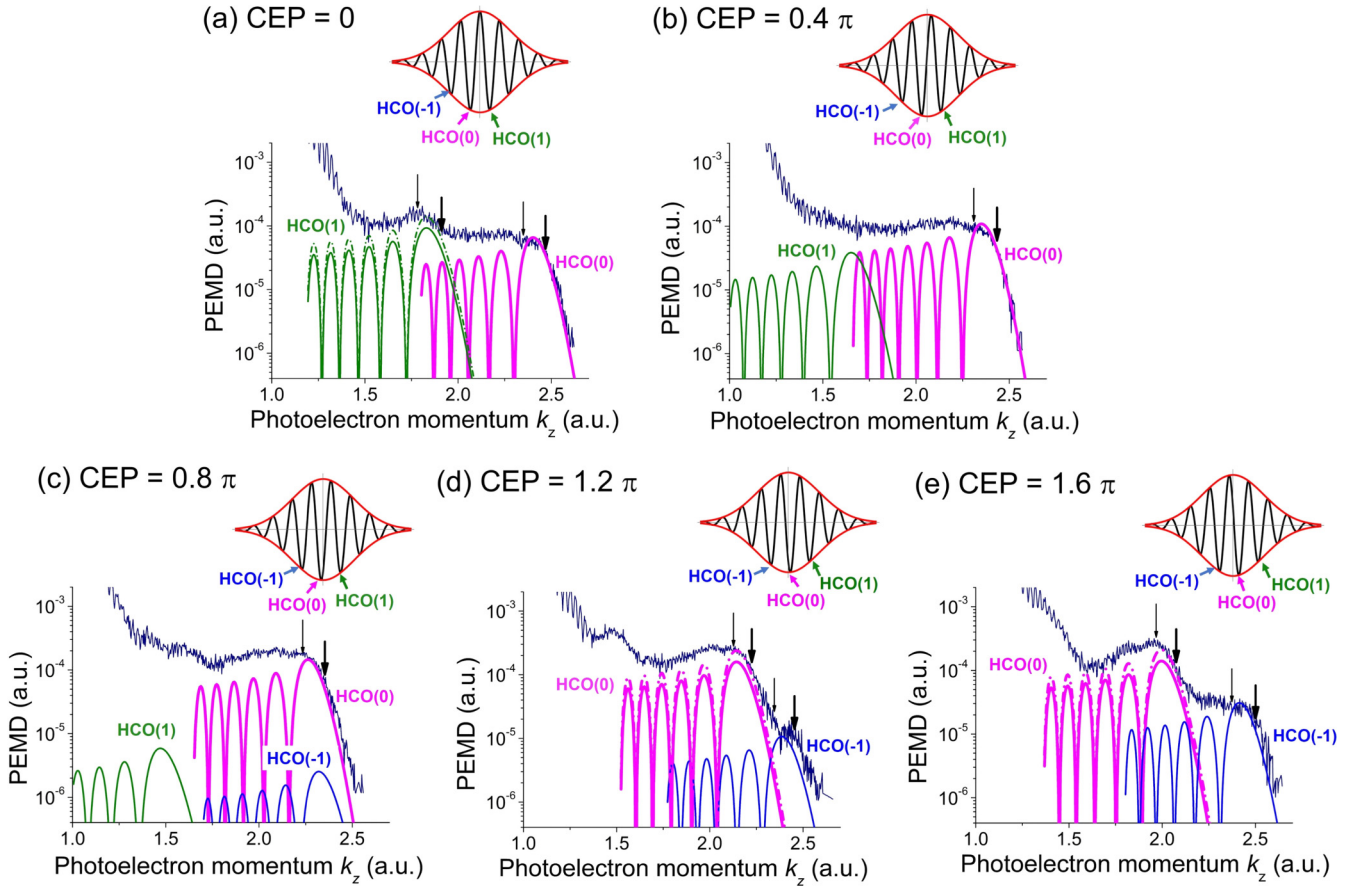


FIG. 6. Same as Fig. 5, but at an estimated intensity of $3.2 \times 10^{13} \text{ W/cm}^2$ and a pulse duration of 13.5 fs. Dash dotted curves show $1.5 \times P_c(k_z)$. Note that we set a common range in the vertical axis for better comparison, which makes blue (dark gray) and green (light gray) curves out of range in some cases.

of 0.0, 0.4, 0.8, 1.2, and $1.6 \times \pi$ at the estimated intensities I of $2.6 \times 10^{13} \text{ W/cm}^2$ ($F_0 = 0.02722$ a.u.) and $3.2 \times 10^{13} \text{ W/cm}^2$ ($F_0 = 0.03028$ a.u.), respectively. The contribution from a different half cycle to a PEMD is separated in energy. As discussed in Sec. IV A, the intensity and duration of the field are estimated by using measured PEMDs in the vicinity of outermost HCOs for the CEP in the range of $-0.3\pi \leq \phi \leq 0.7\pi$, corresponding to HCO(0) at $0 \leq \phi \leq 0.7\pi$ and HCO(-1) at $1.7\pi \leq \phi \leq 2.0\pi$. This limited CEP range allows us to compare the measured PEMDs $P(k_z)$ and calculated PEMDs $P_c(k_z)$ in the other regions. Hence we can confirm the validity of the adiabatic theory and quantum shift. Using these field parameters, we calculate three PEMDs $P_c(k_z)$ from different half cycles as shown in blue, red, and green curves. Note that the insets of Figs. 5 and 6 show the corresponding half cycles to three dominant HCOs defined as HCO(-1), HCO(0), and HCO(1).

Now we will make a quantitative comparison between the measured PEMDs $P(k_z)$ and calculated PEMDs $P_c(k_z)$. For the data of Figs. 5 and 6, we only use the measured PEMDs around the outermost HCO in the upper panels (a),(b) to determine the intensity and duration. In these panels, as shown in Figs. 5(a) and 5(b), the measured PEMDs around the outermost HCO [HCO(0)] agree with $P_c(k_z)$ including the exponential decay for two orders of magnitude. The existence

of two other HCOs [HCO(-1), HCO(1)] is consistent with the observation. Especially in Fig. 5(a), the peak structure at 1.6 a.u. is well reproduced by the cutoff peak of HCO(1). Figure 5(c) shows that the measured PEMD around the outermost HCO [HCO(0)] is also in good agreement with $P_c(k_z)$. In Figs. 5(d) and 5(e), the observed double-knee structures agree well with two HCOs [HCO(-1) and HCO(0)] in their positions and relative yields. It is noteworthy that we do not use the measured PEMDs $P(k_z)$ in Figs. 5(c)–5(e) to estimate the field parameters. This high degree of agreement of multiple HCOs between the adiabatic theory and experiments demonstrates the quantum shift of caustics.

Similar to Fig. 5, the data in Fig. 6 can be understood by the CEP-dependent interrelation of multiple HCOs. In Figs. 6(a)–6(c), the exponential decays are well reproduced. The observed peak in Fig. 6(a) at 1.7 a.u. is also reproduced by HCO(1). In Figs. 6(d) and 6(e), the positions of double-knee structure are reproduced by HCO(-1) and HCO(0) except for the relative yields of the HCOs. Meanwhile, the relative yields of several inner HCOs seem to be underestimated by the adiabatic theory. The dash-dotted curves in Figs. 6(a), 6(d), and 6(e) are $1.5 \times P_c(k_z)$ that agree better to $P(k_z)$ than $P_c(k_z)$. This small discrepancy of relative yields in the inner HCO may arise from the coherent sum of contributions from different half cycles in the PEMD, or may be due to many-electron,

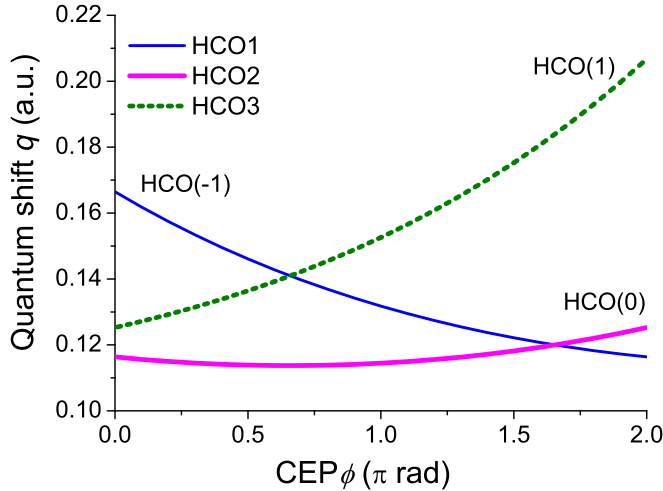


FIG. 7. Quantum shift q as a function of the CEP ϕ for three HCOs at an intensity of 2.6×10^{13} W/cm² and a pulse duration of 13.8 fs. The definition of HCO(n) is mentioned in Sec. IV.

spin-orbit coupling, and nonadiabatic coupling effects. Although these effects may be studied in the future, they are out of the scope of the present study.

The quantum shift q given in Eq. (3) is considerably different for individual half cycles. Figure 7 shows the CEP-dependent q calculated using Eq. (3) for three different HCOs. As mentioned before, the positions of HCOs in the measured PEMDs are well reproduced by the adiabatic theory including the quantum shift. We thus conclude that the quantum shift of the caustic is experimentally verified. Note that the shift q is hardly affected by Stark effect in our experimental conditions. At most the difference between $E(F(t_i))$ and E_0 is less than 0.002 a.u. at the present pulse amplitudes. In the long-wavelength limit at a fixed field strength, the quantum shift q will become zero, and the quantum caustic coincides with the classical caustic.

C. Focal volume effect

The measured PEMD $P(k_z)$ near the HCO is reproduced by $P_c(k_z)$ with the single estimated intensity I . This means that the volume effect on $P(k_z)$ near the HCOs and the position of the caustic is negligible under our experimental conditions. In contrast to the vicinity of the HCO, obtained $P(k_z)$ in the lower energy side of k_c is not reproduced by $P_c(k_z)$ via Eq. (4) using a single effective intensity. The calculated $P_c(k_z)$ shows clear oscillation because of the interference between the contributions from the long and short classical trajectories, as shown in Figs. 5 and 6. However, in the obtained PEMDs, such an oscillation behavior cannot be observed, which implies that the focal volume effect heavily affects $P(k_z)$ obtained in the lower energy side of k_c based on the intensity distribution with respect to the interaction volume. Therefore, we model the intensity and target distributions in the focal area to elucidate the discrepancy between the measured $P(k_z)$ and calculated $P_c(k_z)$ below k_c . As mentioned in Sec. III, to avoid the change of the CEP due to the Gouy phase effect, the target position is offset from the focal point with a loose focusing geometry. The CEP and intensity distribution along the propagation

direction, which is defined as the x axis, change very slowly. Therefore, we only consider the focal volume effect in the yz plane. We assume the Gaussian beam mode whose intensity distribution $I(\rho)$ expressed as

$$I(\rho) = I_0 \exp[-2(\rho/W)^2], \quad (7)$$

where ρ is the distance from the beam axis, and the spot radius ($1/e^2$) W is estimated to be $127 \mu\text{m}$ under our experimental condition. Based on an effusive flow from a reservoir through a small aperture (nozzle) with infinitesimal thickness [62], we assume that the target flow is generated from a point source at $(y, z) = (-300 \mu\text{m} - d_{\text{nozzle}}, 0)$ in the nozzle. Here, the nozzle tip is set at $(y, z) = (-300 \mu\text{m}, 0)$ and the nozzle diameter $d_{\text{nozzle}} = 30 \mu\text{m}$ is introduced to include the effect of the finite size of a small aperture. The distribution of target gas $D(R, \theta)$ is then approximately expressed by

$$\begin{aligned} D(R, \theta) &\propto \cos/R^2 \quad (-300 \mu\text{m} < y < \infty) \\ &= 0 \quad (y < -300 \mu\text{m}), \end{aligned} \quad (8)$$

where R is the distance from the point source given by $R = \sqrt{(y + 300 \mu\text{m} + d_{\text{nozzle}})^2 + z^2}$ and θ is the angle from the nozzle axis expressed by $\cos \theta = (y + 300 \mu\text{m} + d_{\text{nozzle}})/R$. We assume that there is no gas flow in the back side of the nozzle tip in the above equation. Using the gas density, the focal volume averaged PEMD $\bar{P}_c(k_z)$ is given by

$$\bar{P}_c(k_z) \sim \int P_c(k_z) D(R, \theta) dy dz, \quad (9)$$

where the spatial dependence of $P_c(k_z)$ is evaluated through its intensity dependence and the laser intensity distribution in Eq. (7).

Figure 8 shows the measured $P(k_z)$ and calculated $P_c(k_z)$ and $\bar{P}_c(k_z)$ with and without the focal volume effect, respectively, at $\phi = 0$. The measured PEMD $P(k_z)$ is well reproduced by the calculated $\bar{P}_c(k_z)$ considering the volume effect at a peak intensity I_0 of 2.71×10^{13} W/cm² even in the lower energy side of the classical caustic. The interference pattern becomes very weak because of the volume effect. The calculation of the volume effect by assuming uniform distribution of target gas is almost identical with that by Eq. (8) under our experimental condition. The nozzle position is as close to the focal spot as possible unless photoemission occurs from a nozzle. This result implies that the target distribution can be approximately considered to be a uniform distribution in the case of the effusive source.

D. Extraction of DCSs around the caustic

The laser parameters, elastic scattering differential cross sections, and tunneling ionization rate of a target are encoded in PEMDs $P(k_z)$. Such information can be extracted from $P(k_z)$ based on the adiabatic theory. Here, we propose an extraction scheme of the backscattering differential cross sections (DCSs) from PEMDs around the caustic. The first step is pulse characterization from measured PEMDs near HCOs. As mentioned before, we determine the laser parameters by using the fitting procedure as described in the Appendix. This procedure allows us to accurately determine the laser parameters, resulting in precise calculations of the positions of the classical k_c and quantum k_q caustic, the returning wave

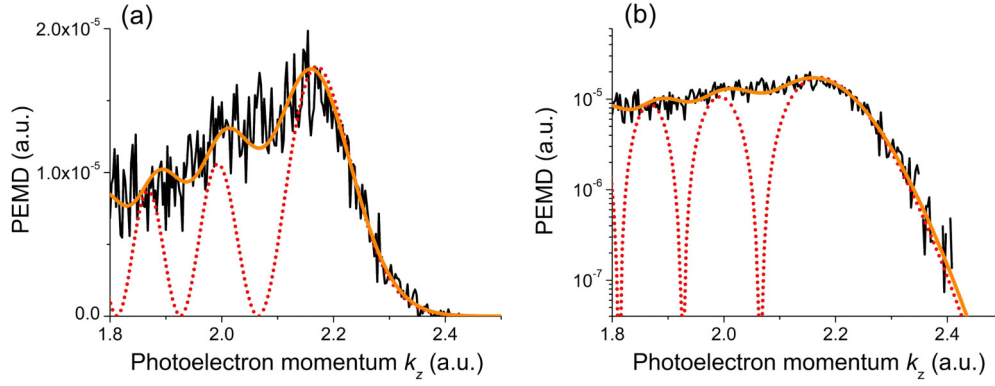


FIG. 8. Measured (thin black) $P(k_z)$ and calculated (dotted red) PEMDs $P_c(k_z)$ by Eq. (4) at $\phi = 0$ at a pulse duration of 13.8 fs when considering an effective intensity of 2.6×10^{13} W/cm². These curves are identical to the curves shown in Fig. 5(a). Thick orange curves represent the calculated PEMDs $\bar{P}_c(k_z)$ based on the intensity and target density distribution given by Eqs. (7)–(9) at $I_0 = 2.71 \times 10^{13}$ W/cm² with (a) linear and (b) logarithmic scales.

packet $W(k_z)$, and the rescattering momentum u_f . For the next step, we divide measured PEMD $P(k_z)$ by calculated returning wave packet $W(k_z)$ using the estimated parameters, which is a DCS, $|f(|u_f|, \pi)|^2$, using Eq. (4). This extraction scheme of a DCS is based on the assumption that a calculated $W(k_z)$ is correct. In other words, we assume that the discrepancy between measured and calculated PEMDs originates from an error of a DCS. We use only PEMDs around HCO(0) in the CEP range of $\phi = 0$ to 2π , because PEMDs around HCO(± 1)s are poor statistics. As for the CEP range of $\phi = 0$ to 0.7π , in order to obtain the DCS, we average $P(k_z)/W(k_z)$ in the k_z range of $k_z > k_p$, where k_p is the calculated peak position near the HCO, which is the same range as the fitting procedure in the Appendix. In the other CEP range of $\phi = 0.8\pi$ to 2π , we also use the same k_z range to obtain the DCS. If a PEMD shows two HCO structures, in addition to the condition of $k_z > k_p$, we restrict k_z below the knee structure that corresponds to the outer HCO to eliminate the contribution of the outer HCO to the PEMD. The present scheme can allow us to achieve better statistics than the previous scheme [44] because we use not only an electron yield $P(k_z)$ at k_c but also distribution $P(k_z)$ in the vicinity of the caustic.

Figure 9 presents the extracted and calculated DCSs of Xe⁺ ions. The extracted DCSs agree with the calculated DCSs based on the single active electron approximation within an error of approximately 50%, corresponding to the discrepancy between measured and calculated PEMDs. It should be noted again that the normalization factor is an unknown parameter. The estimated normalization factor depends on the used CEP range for fitting procedure. Thus, in the higher-rescattering momentum side, extracted DCSs agree with calculated DCSs, because these corresponding CEPs are used for fitting. If the normalization factor is multiplied by 0.7, an extracted DCS is also changed to be $0.7 \times |f(|u_f|, \pi)|^2$. Figure 9 also shows $0.7 \times |f(|u_f|, \pi)|^2$ for an estimated field amplitude F_0 of 0.03028 a.u. One can see clearly that the relative behavior of extracted DCSs as a function of the rescattering momentum u_f is well reproduced by calculations. In the case of a shorter infrared pulse, the contribution of the outer caustics to a PEMD in the vicinity of an inner caustic becomes negligibly small [44]. Thus an ultrashort pulse is advantageous to accurately extract a DCS from a PEMD.

V. CONCLUSIONS

We experimentally and theoretically explored the rescattering PEMDs of a Xe atom near the HCOs using CEP stable few-cycle infrared pulses. The CEP-stable pulses enable us to identify the contribution of each half cycle to a PEMD. The observed CEP dependence of the PEMDs around HCOs is well reproduced by the analytical factorization formula that is derived from the adiabatic theory including the quantum shift of caustics [36]. This means that the existence of quantum caustics is experimentally verified. Meanwhile, in the present experiment we could not resolve oscillations in the plateau region on the lower-energy side of the caustic, induced by the interference between the long and short trajectories, because of the focal volume effect. These results indicate that HCOs for few-cycle pulses can be used to quantitatively define the quantum and classical caustics, which are associated with only one rescattering momentum u_f . Recent rescattering experiments at 3.1 μm show the evidence of multiple returns [63], which can be treated by the adiabatic theory with a

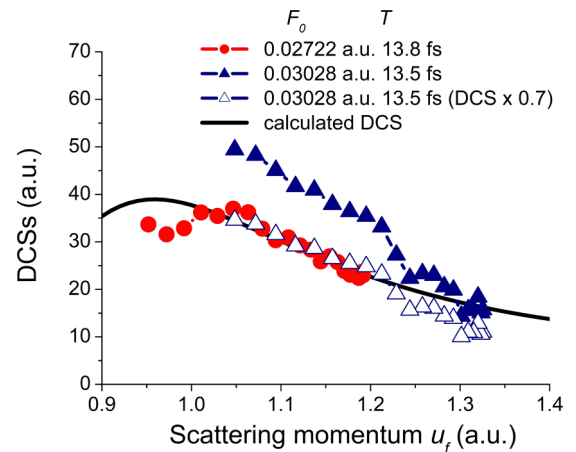


FIG. 9. Extracted DCSs $|f(|u_f|, \pi)|^2$ of Xe⁺ for estimated field amplitudes F_0 of 0.02722 (circle) and 0.03028 a.u. (closed triangle) as a function of the rescattering momentum u_f . The open triangle shows $0.7 \times |f(|u_f|, \pi)|^2$ for F_0 of 0.03028 a.u. The black curve represents calculated DCSs $|f(|u_f|, \pi)|^2$.

different quantum shift for each return. The CEP mapping method [44] with the adiabatic theory [36,51] allows one to extract well-defined elastic scattering processes from rescattered PEMDs, which opens an opportunity to examine the production of vortex electrons [64]. It can also be used to verify an extended adiabatic theory in the future that includes multielectron effects or spin-orbit coupling.

ACKNOWLEDGMENTS

We thank K. Takeuchi, T. Yang, and Dr. T. Kurihara for helpful discussions. This research was in part supported by Grant-in-Aid for Scientific Research (S) Grant No. 18H05250 and Scientific Research (C) Grant No. 20K05358 of the Japan Society for the Promotion of Science. We acknowledge support by the German Research Foundation via Project No. KI-1439/10-1, LMUexcellent, and the excellence cluster “Munich Center for Advanced Photonics (MAP).” M.F.K. is grateful for support by the Max Planck Society via their Fellow program.

APPENDIX: FITTING PROCEDURE FOR DETERMINATION OF THE LASER PARAMETERS AND THE NORMALIZATION FACTOR

By fitting the measured PEMD $P(k_z)$ to the calculated PEMD $P_c(k_z)$ from a given half cycle by Eq. (4) near the outermost HCO, we determine the laser parameters and the

normalization factor N of $P(k_z)$ to $P_c(k_z)$. To evaluate the fitting quality, we introduce the weighted sum of squared errors R , which is given by

$$R = \sum_{\phi} \sum_{k_z > k_p} \left[\frac{NP(k_z) - P_c(k_z)}{|P(k_z)|^{1/2}} \right]^2, \quad (\text{A1})$$

where k_p represents the calculated peak position near the outermost HCO. Moreover, we exclude measured PEMD $P(k_z)$ below a yield of 10^5 from fitting procedure due to poor statistics and background noise. While $P(k_z)$ only depends on the CEP ϕ , $P_c(k_z)$ depends on the CEP ϕ , the intensity I , and the pulse duration T . The weight function is $P(k_z)^{1/2}$, corresponding to the statistical error. The function R is mostly based on the Chi-square fitting procedure. We just replaced a standard deviation with $P(k_z)^{1/2}$. We use a limited CEP range of $\phi = -0.3\pi$ to 0.7π , corresponding to the range of $\phi = 0$ to 0.7π and $\phi = 1.7\pi$ to 2.0π because of the 2π periodicity of $P(k_z)$, and PEMDs at $k_z > k_p$, for fitting procedure. We seek the minimum value of R with fitting parameters I , T , and N . Based on this fitting procedure, the field intensity I and the pulse duration T for two experimental cases with the pulse energies of 190 and 210 μJ are estimated to be $I = 2.6 \times 10^{13} \text{ W/cm}^2$ ($F_0 = 0.02722$ a.u.) with $T = 13.8$ fs and $3.2 \times 10^{13} \text{ W/cm}^2$ ($F_0 = 0.03028$ a.u.) with $T = 13.5$ fs, respectively.

-
- [1] P. B. Corkum, Plasma Perspective on Strong Field Multiphoton Ionization, *Phys. Rev. Lett.* **71**, 1994 (1993).
- [2] P. B. Corkum and F. Krausz, Attosecond science, *Nat. Phys.* **3**, 381 (2007).
- [3] R. Kienberger, E. Goulielmakis, M. Uiberacker, A. Baltuska, V. Yakovlev, F. Bammer, A. Scrinzi, T. Westerwalbesloh, U. Kleineberg, U. Heinzmann, M. Drescher, and F. Krausz, Atomic transient recorder, *Nature (London)* **427**, 817 (2004).
- [4] G. Sansone, E. Benedetti, F. Calegari, C. Vozzi, L. Avaldi, R. Flammini, L. Poletto, P. Villoresi, C. Altucci, R. Velotta, S. Stagira, S. De Silvestri, and M. Nisoli, Isolated single-cycle attosecond pulses, *Science* **314**, 443 (2006).
- [5] J. Itatani, J. Levesque, D. Zeidler, H. Niikura, H. Pépin, J. C. Kieffer, P. B. Corkum, and D. M. Villeneuve, Tomographic imaging of molecular orbitals, *Nature (London)* **432**, 867 (2004).
- [6] S. Baker, J. S. Robinson, C. A. Haworth, H. Teng, R. A. Smith, C. C. Chirilă, M. Lein, J. W. G. Tisch, and J. P. Marangos, Probing proton dynamics in molecules on an attosecond time scale, *Science* **312**, 424 (2006).
- [7] H. J. Wörner, J. B. Bertrand, D. V. Kartashov, P. B. Corkum, and D. M. Villeneuve, Following a chemical reaction using high-harmonic interferometry, *Nature (London)* **466**, 604 (2010).
- [8] P. M. Kraus, B. Mignolet, D. Baykusheva, A. Rupenyany, L. Horný, E. F. Penka, G. Grassi, O. I. Tolstikhin, J. Schneider, F. Jensen, L. B. Madsen, A. D. Bandrauk, F. Remacle, and H. J. Wörner, Measurement and laser control of attosecond charge migration in ionized iodoacetylene, *Science* **350**, 790 (2015).
- [9] K. Kaneshima, Y. Ninota, and T. Sekikawa, Time-resolved high-harmonic spectroscopy of ultrafast photoisomerization dynamics, *Opt. Express* **26**, 31039 (2018).
- [10] H. Niikura, F. Légaré, R. Hasbani, A. D. Bandrauk, M. Y. Ivanov, D. M. Villeneuve, and P. B. Corkum, Sub-laser-cycle electron pulses for probing molecular dynamics, *Nature (London)* **417**, 917 (2002).
- [11] A. Staudte, D. Pavičić, S. Chelkowski, D. Zeidler, M. Meckel, H. Niikura, M. Schöffler, S. Schössler, B. Ulrich, P. P. Rajeev, T. Weber, T. Jahnke, D. M. Villeneuve, A. D. Bandrauk, C. L. Cocke, P. B. Corkum, and R. Dörner, Attosecond Stroboscopic of Two-Surface Population Dynamics in Dissociating H_2^+ , *Phys. Rev. Lett.* **98**, 073003 (2007).
- [12] X. Xie, K. Doblhoff-Dier, S. Roither, M. S. Schöffler, D. Kartashov, H. Xu, T. Rathje, G. G. Paulus, A. Baltuška, S. Gräfe, and M. Kitzler, Attosecond-Recollision-Controlled Selective Fragmentation of Polyatomic Molecules, *Phys. Rev. Lett.* **109**, 243001 (2012).
- [13] T. Weber, H. Giessen, M. Weckenbrock, G. Urbasch, A. Staudte, L. Spielberger, O. Jagutzki, V. Mergel, M. Vollmer, and R. Dörner, Correlated electron emission in multiphoton double ionization, *Nature (London)* **405**, 658 (2000).
- [14] A. Staudte, C. Ruiz, M. Schöffler, S. Schössler, D. Zeidler, T. Weber, M. Meckel, D. M. Villeneuve, P. B. Corkum, A. Becker, and R. Dörner, Binary and Recoil Collisions in Strong Field Double Ionization of Helium, *Phys. Rev. Lett.* **99**, 263002 (2007).
- [15] N. Camus, B. Fischer, M. Kremer, V. Sharma, A. Rudenko, B. Bergues, M. Kübel, N. G. Johnson, M. F. Kling, T. Pfeifer,

- J. Ullrich, and R. Moshhammer, Attosecond Correlated Dynamics of Two Electrons Passing through a Transition State, *Phys. Rev. Lett.* **108**, 073003 (2012).
- [16] B. Bergues, M. Kübel, N. G. Johnson, B. Fischer, N. Camus, K. J. Betsch, O. Herrwerth, A. Senftleben, A. M. Saylor, T. Rathje, T. Pfeifer, I. Ben-Itzhak, R. R. Jones, G. G. Paulus, F. Krausz, R. Moshhammer, J. Ullrich, and M. F. Kling, Attosecond tracing of correlated electron-emission in non-sequential double ionization, *Nat. Commun.* **3**, 813 (2012).
- [17] M. Meckel, D. Comtois, D. Zeidler, A. Staudte, D. Pavičić, H. C. Bandulet, H. Pépin, J. C. Kieffer, R. Dörner, D. M. Villeneuve, and P. B. Corkum, Laser-induced electron tunneling and diffraction, *Science* **320**, 1478 (2008).
- [18] R. Gopal, K. Simeonidis, R. Moshhammer, T. Ergler, M. Dürr, M. Kurka, K.-U. Kühnel, S. Tschuch, C.-D. Schröter, D. Bauer, J. Ullrich, A. Rudenko, O. Herrwerth, T. Uphues, M. Schultze, E. Goulielmakis, M. Uiberacker, M. Lezius, and M. F. Kling, Three-Dimensional Momentum Imaging of Electron Wave Packet Interference in Few-Cycle Laser Pulses, *Phys. Rev. Lett.* **103**, 053001 (2009).
- [19] Y. Huismans, A. Rouzée, A. Gijsbertsen, J. H. Jungmann, A. S. Smolkowska, P. S. W. M. Logman, F. Lépine, C. Cauchy, S. Zamith, T. Marchenko, J. M. Bakker, G. Berden, B. Redlich, A. F. G. van der Meer, H. G. Muller, W. Vermin, K. J. Schafer, M. Spanner, M. Y. Ivanov, O. Smirnova *et al.*, Time-resolved holography with photoelectrons, *Science* **331**, 61 (2011).
- [20] X.-B. Bian and A. D. Bandrauk, Attosecond Time-Resolved Imaging of Molecular Structure by Photoelectron Holography, *Phys. Rev. Lett.* **108**, 263003 (2012).
- [21] D. D. Hickstein, P. Ranitovic, S. Witte, X.-M. Tong, Y. Huismans, P. Arpin, X. Zhou, K. E. Keister, C. W. Hogle, B. Zhang, C. Ding, P. Johnsson, N. Toshima, M. J. J. Vrakking, M. M. Murnane, and H. C. Kapteyn, Direct Visualization of Laser-Driven Electron Multiple Scattering and Tunneling Distance in Strong-Field Ionization, *Phys. Rev. Lett.* **109**, 073004 (2012).
- [22] Y. Zhou, O. I. Tolstikhin, and T. Morishita, Near-Forward Rescattering Photoelectron Holography in Strong-Field Ionization: Extraction of the Phase of the Scattering Amplitude, *Phys. Rev. Lett.* **116**, 173001 (2016).
- [23] G. Porat, G. Alon, S. Rozen, O. Pedatzur, M. Krüger, D. Azoury, A. Natan, G. Orenstein, B. D. Bruner, M. J. J. Vrakking, and N. Dudovich, Attosecond time-resolved photoelectron holography, *Nat. Commun.* **9**, 2805 (2018).
- [24] G. G. Paulus, W. Becker, W. Nicklich, and H. Walther, Rescattering effects in above-threshold ionization: A classical model, *J. Phys. B* **27**, L703 (1994).
- [25] D. B. Milošević, G. G. Paulus, and W. Becker, High-order above-threshold ionization with few-cycle pulse: A meter of the absolute phase, *Opt. Express* **11**, 1418 (2003).
- [26] G. G. Paulus, F. Lindner, H. Walther, A. Baltuška, E. Goulielmakis, M. Lezius, and F. Krausz, Measurement of the Phase of Few-Cycle Laser Pulses, *Phys. Rev. Lett.* **91**, 253004 (2003).
- [27] D. B. Milošević, G. G. Paulus, D. Bauer, and W. Becker, Above-threshold ionization by few-cycle pulses, *J. Phys. B: At., Mol., Opt. Phys.* **39**, R203 (2006).
- [28] T. Wittmann, B. Horvath, W. Helml, M. G. Schätzel, X. Gu, A. L. Cavalieri, G. G. Paulus, and R. Kienberger, Single-shot carrier-envelope phase measurement of few-cycle laser pulses, *Nat. Phys.* **5**, 357 (2009).
- [29] M. F. Kling, J. Rauschenberger, A. J. Verhoef, E. Hascović, T. Uphues, D. B. Milošević, H. G. Muller, and M. J. J. Vrakking, Imaging of carrier-envelope phase effects in above-threshold ionization with intense few-cycle laser fields, *New J. Phys.* **10**, 025024 (2008).
- [30] S. Fukahori, T. Ando, S. Miura, R. Kanya, K. Yamanouchi, T. Rathje, and G. G. Paulus, Determination of the absolute carrier-envelope phase by angle-resolved photoelectron spectra of Ar by intense circularly polarized few-cycle pulses, *Phys. Rev. A* **95**, 053410 (2017).
- [31] T. Morishita, A.-T. Le, Z. Chen, and C. D. Lin, Accurate Retrieval of Structural Information from Laser-Induced Photoelectron and High-Order Harmonic Spectra by Few-Cycle Laser Pulses, *Phys. Rev. Lett.* **100**, 013903 (2008).
- [32] M. V. Frolov, N. L. Manakov, and A. F. Starace, Analytic formulas for above-threshold ionization or detachment plateau spectra, *Phys. Rev. A* **79**, 033406 (2009).
- [33] A. Čerkić, E. Hasović, D. B. Milošević, and W. Becker, High-order above-threshold ionization beyond the first-order Born approximation, *Phys. Rev. A* **79**, 033413 (2009).
- [34] O. I. Tolstikhin, T. Morishita, and S. Watanabe, Adiabatic theory of ionization of atoms by intense laser pulses: One-dimensional zero-range-potential model, *Phys. Rev. A* **81**, 033415 (2010).
- [35] M. V. Frolov, D. V. Knyazeva, N. L. Manakov, A. M. Popov, O. V. Tikhonova, E. A. Volkova, M.-H. Xu, L.-Y. Peng, L.-W. Pi, and A. F. Starace, Validity of Factorization of the High-Energy Photoelectron Yield in Above-Threshold Ionization of an Atom by a Short Laser Pulse, *Phys. Rev. Lett.* **108**, 213002 (2012).
- [36] T. Morishita and O. I. Tolstikhin, Adiabatic theory of strong-field photoelectron momentum distributions near a backward rescattering caustic, *Phys. Rev. A* **96**, 053416 (2017).
- [37] M. Okunishi, T. Morishita, G. Prümper, K. Shimada, C. D. Lin, S. Watanabe, and K. Ueda, Experimental Retrieval of Target Structure Information from Laser-Induced Rescattered Photoelectron Momentum Distributions, *Phys. Rev. Lett.* **100**, 143001 (2008).
- [38] D. Ray, B. Ulrich, I. Bocharova, C. Maharjan, P. Ranitovic, B. Gramkow, M. Magrakvelidze, S. De, I. V. Litvinyuk, A. T. Le, T. Morishita, C. D. Lin, G. G. Paulus, and C. L. Cocke, Large-Angle Electron Diffraction Structure in Laser-Induced Rescattering from Rare Gases, *Phys. Rev. Lett.* **100**, 143002 (2008).
- [39] S. Mischeau, Z. Chen, A. T. Le, J. Rauschenberger, M. F. Kling, and C. D. Lin, Accurate Retrieval of Target Structures and Laser Parameters of Few-Cycle Pulses from Photoelectron Momentum Spectra, *Phys. Rev. Lett.* **102**, 073001 (2009).
- [40] D. B. Milošević, W. Becker, M. Okunishi, G. Prümper, K. Shimada, and K. Ueda, Strong-field electron spectra of rare-gas atoms in the rescattering regime: Enhanced spectral regions and a simulation of the experiment, *J. Phys. B* **43**, 015401 (2009).
- [41] C. I. Blaga, J. Xu, A. D. DiChiara, E. Sistrunk, K. Zhang, P. Agostini, T. A. Miller, L. F. DiMauro, and C. D. Lin, Imaging ultrafast molecular dynamics with laser-induced electron diffraction, *Nature (London)* **483**, 194 (2012).
- [42] J. Xu, C. I. Blaga, A. D. DiChiara, E. Sistrunk, K. Zhang, Z. Chen, A.-T. Le, T. Morishita, C. D. Lin, P. Agostini, and

- L. F. DiMauro, Laser-Induced Electron Diffraction for Probing Rare Gas Atoms, *Phys. Rev. Lett.* **109**, 233002 (2012).
- [43] B. Wolter, M. G. Pullen, M. Baudisch, M. Sclafani, M. Hemmer, A. Senftleben, C. D. Schröter, J. Ullrich, R. Moshhammer, and J. Biegert, Strong-Field Physics with Mid-IR Fields, *Phys. Rev. X* **5**, 021034 (2015).
- [44] H. Geiseler, N. Ishii, K. Kaneshima, F. Geier, T. Kanai, O. I. Tolstikhin, T. Morishita, and J. Itatani, Carrier-envelope phase mapping in laser-induced electron diffraction, *Phys. Rev. A* **94**, 033417 (2016).
- [45] B. Wolter, M. G. Pullen, A.-T. Le, M. Baudisch, K. Doblhoff-Dier, A. Senftleben, M. Hemmer, C. D. Schröter, J. Ullrich, T. Pfeifer, R. Moshhammer, S. Gräfe, O. Vendrell, C. D. Lin, and J. Biegert, Ultrafast electron diffraction imaging of bond breaking in di-ionized acetylene, *Science* **354**, 308 (2016).
- [46] S. G. Walt, N. Bhargava Ram, M. Atala, N. I. Shvetsov-Shilovski, A. von Conta, D. Baykusheva, M. Lein, and H. J. Wörner, Dynamics of valence-shell electrons and nuclei probed by strong-field holography and rescattering, *Nat. Commun.* **8**, 15651 (2017).
- [47] Y. Ito, M. Okunishi, T. Morishita, O. I. Tolstikhin, and K. Ueda, Rescattering photoelectron spectroscopy of heterodiatomic molecules with an analytical returning photoelectron wave packet, *Phys. Rev. A* **97**, 053411 (2018).
- [48] K. Amini, M. Sclafani, T. Steinle, A.-T. Le, A. Sanchez, C. Müller, J. Steinmetzer, L. Yue, J. R. Martínez Saavedra, M. Hemmer, M. Lewenstein, R. Moshhammer, T. Pfeifer, M. G. Pullen, J. Ullrich, B. Wolter, R. Moszynski, F. J. García de Abajo, C. D. Lin, S. Gräfe *et al.*, Imaging the Renner–Teller effect using laser-induced electron diffraction, *Proc. Natl. Acad. Sci. USA* **116**, 8173 (2019).
- [49] M. Okunishi, Y. Ito, V. Sharma, S. Aktar, K. Ueda, R. R. Lucchese, A. I. Dnestryan, O. I. Tolstikhin, S. Inoue, H. Matsui, and T. Morishita, Rescattering photoelectron spectroscopy of the CO₂ molecule: Progress towards experimental discrimination between theoretical target-structure models, *Phys. Rev. A* **100**, 053404 (2019).
- [50] N. Ishii, K. Kaneshima, K. Kitano, T. Kanai, S. Watanabe, and J. Itatani, Sub-two-cycle, carrier-envelope phase-stable, intense optical pulses at 1.6 μm from a BiB₃O₆ optical parametric chirped-pulse amplifier, *Opt. Lett.* **37**, 4182 (2012).
- [51] O. I. Tolstikhin and T. Morishita, Adiabatic theory of ionization by intense laser pulses: Finite-range potentials, *Phys. Rev. A* **86**, 043417 (2012).
- [52] M. Lewenstein, P. Balcou, M. Y. Ivanov, A. L’Huillier, and P. B. Corkum, Theory of high-harmonic generation by low-frequency laser fields, *Phys. Rev. A* **49**, 2117 (1994).
- [53] M. V. Frolov, N. L. Manakov, T. S. Sarantseva, and A. F. Starace, Analytic formulae for high harmonic generation, *J. Phys. B* **42**, 035601 (2009).
- [54] Y. Okajima, O. I. Tolstikhin, and T. Morishita, Adiabatic theory of high-order harmonic generation: One-dimensional zero-range-potential model, *Phys. Rev. A* **85**, 063406 (2012).
- [55] E. Pisanty, M. F. Ciappina, and M. Lewenstein, The imaginary part of the high-harmonic cutoff, *J. Phys.: Photonics* **2**, 034013 (2020).
- [56] P. A. Batishchev, O. I. Tolstikhin, and T. Morishita, Atomic Siegert states in an electric field: Transverse momentum distribution of the ionized electrons, *Phys. Rev. A* **82**, 023416 (2010).
- [57] V. H. Trinh, O. I. Tolstikhin, L. B. Madsen, and T. Morishita, First-order correction terms in the weak-field asymptotic theory of tunneling ionization, *Phys. Rev. A* **87**, 043426 (2013).
- [58] L. D. Landau and E. M. Lifshitz, *Quantum Mechanics, Non-Relativistic Theory* (Pergamon, Oxford, 1977).
- [59] R. Kopold, D. B. Milošević, and W. Becker, Rescattering Processes for Elliptical Polarization: A Quantum Trajectory Analysis, *Phys. Rev. Lett.* **84**, 3831 (2000).
- [60] P. Salières, B. Carré, L. Le Déroff, F. Grasbon, G. G. Paulus, H. Walther, R. Kopold, W. Becker, D. B. Milošević, A. Sanpera, and M. Lewenstein, Feynman’s path-integral approach for intense-laser-atom interactions, *Science* **292**, 902 (2001).
- [61] M. Busuladžić, A. Gazibegović-Busuladžić, and D. B. Milošević, High-order above-threshold ionization in a laser field: Influence of the ionization potential on the high-energy cutoff, *Laser Phys.* **16**, 289 (2006).
- [62] G. Sanna and G. Tomassetti, *Introduction of Molecular Beams Gas Dynamics* (Imperial College Press, London, 2005).
- [63] M. Kübel, P. Wustelt, Y. Zhang, S. Skruszewicz, D. Hoff, D. Würzler, H. Kang, D. Zille, D. Adolph, G. G. Paulus, A. M. Saylor, M. Dumergue, A. Nayak, R. Flender, L. Haizer, M. Kurucz, B. Kiss, S. Kühn, B. Fetić, and D. B. Milošević, High-Order Phase-Dependent Asymmetry in the Above-Threshold Ionization Plateau, *Phys. Rev. Lett.* **126**, 113201 (2021).
- [64] O. I. Tolstikhin and T. Morishita, Strong-field ionization, rescattering, and target structure imaging with vortex electrons, *Phys. Rev. A* **99**, 063415 (2019).